Structural Chemistry
https://doi.org/10.1007/s11224-025-02555-x

RESEARCH

Piperazine-thiophene hybrid as a promising SGLT2 inhibitor: insights from DFT and molecular docking studies

Özlem Gündoğdu Aytaç[1] · Abdurrahman Atalay[2] · Ebrar Nur Özkan[3] · Sertan Aytaç[1]

Received: 16 May 2025 / Accepted: 23 June 2025

Abstract

The compound 1-(piperazin-1-yl)-2-(thiophen-2-yl) ethan-1-one (**PT**) was comprehensively investigated through computational and molecular docking approaches to evaluate its structural, electronic, and pharmacological properties. Density functional theory (DFT) calculations at the B3LYP/cc-pVDZ level were employed to optimize molecular geometry and analyze electronic descriptors, including frontier molecular orbitals (FMOs), global reactivity parameters, and dipole moments in both gas and solvent phases. **PT** demonstrated moderate chemical stability, high nucleophilicity, and low electrophilicity, suggesting potential for biological activity. Non-linear optical (NLO) properties and UV-spectra computed via time-dependent DFT (TD-DFT) revealed strong solvent dependence and enhanced polarizability, particularly in polar environments. Molecular electrostatic potential (MEP), electron localization function (ELF), and localized orbital locator (LOL) analyses provided deeper insights into reactive sites and electron distribution. Furthermore, natural population analysis (NPA), Mulliken charge distribution, and natural bond orbital (NBO) analyses confirmed intramolecular charge delocalization and stabilizing donor–acceptor interactions. Finally, molecular docking simulations revealed favorable binding of **PT** to the human SGLT2-MAP17 protein complex (PDB ID: 8HEZ), with a binding energy of −6.93 kcal/mol and multiple stabilizing noncovalent interactions. These findings suggest that **PT** could serve as a promising lead compound for SGLT2 inhibition and warrant further pharmacological evaluation.

Keywords Piperazin · Density functional theory · SGLT2 · Molecular docking

Introduction

Type 2 diabetes mellitus (T2DM) remains one of the most prevalent and pressing metabolic disorders worldwide, currently affecting approximately 13.5% of the global population [1–3]. As the incidence of T2DM continues to climb, its contribution to long-term complications particularly chronic kidney disease (CKD), cardiovascular events, infections, and diminished quality of life has become increasingly evident [4–8]. The primary goal in T2DM management is to achieve optimal glycemic control to prevent or delay these complications. Although conventional oral hypoglycemic agents have long played a central role in treatment, their effectiveness in preserving renal function remains limited. In recent years, sodium-glucose cotransporter-2 (SGLT2) inhibitors have emerged as a novel therapeutic option specifically for individuals with T2DM [9–12]. These agents lower blood glucose levels by inhibiting glucose reabsorption in the proximal renal tubules, thereby promoting glycosuria and facilitating the attainment of target hemoglobin A1c (HbA1c) levels [13, 14]. Notably, their clinical benefits extend beyond glycemic control, offering additional protective effects, particularly in renal and cardiovascular health. Importantly, their clinical utility extends beyond glycemic control.

SGLT2 inhibitors also reduce sodium reabsorption in the proximal tubules, leading to increased urinary sodium excretion [15]. This process activates the tubuloglomerular feedback mechanism, thereby decreasing glomerular hyperfiltration, a key contributor to proteinuria, and declining renal

✉ Özlem Gündoğdu Aytaç
ogundogdu@ahievran.edu.tr

[1] Food Processing Department, Kaman Vocational School, Kırşehir Ahi Evran University, 40300 Kaman, Kırşehir, Turkey

[2] Department of Nutrition and Dietetics, Faculty of Health Science, Avrasya University, Trabzon, Turkey

[3] Department of Chemistry, Faculty of Science, Atatürk University, 25240 Yakutiye, Erzurum, Turkey

Published online: 05 July 2025

function in T2DM [16]. By mitigating these pathophysiological changes, SGLT2 inhibitors offer significant nephroprotective effects [17]. Furthermore, strong clinical evidence supports their cardiovascular benefits, particularly in reducing the risk of heart failure and atherosclerotic events in T2DM populations [18, 19]. Consequently, updated clinical guidelines now recommend SGLT2 inhibitors as a first-line therapy for T2DM patients. Given their therapeutic significance, the discovery of novel SGLT2 inhibitors remains a critical pursuit. Based on this rationale, the present study investigated the potential of 1-(piperazin-1-yl)−2-(thiophen-2-yl) ethan-1-one (**PT**) as a candidate SGLT2 inhibitor. Various theoretical parameters were analyzed, including frontier molecular orbitals (FMOs), global reactivity parameters (GRPs), non-linear optical (NLO) responses, and natural bond orbital (NBO) characteristics. Complementary evaluations were also performed, encompassing molecular electrostatic potential (MEP), electron localization function (ELF), Fukui function, and localized orbital locator (LOL).

Computational methods

All computational analyses of the compound 1-(piperazin-1-yl)−2-(thiophen-2-yl)ethan-1-one (**PT**) were carried out using density functional theory (DFT) within the framework of the B3LYP functional [20, 21] and the correlation-consistent polarized valence double-zeta (cc-pVDZ) basis set. Geometry optimization, frequency calculations, and electronic structure analyses were performed using the Gaussian 16 software package [22]. No imaginary frequencies were observed, confirming the structures to be local minima on the potential energy surface. The HOMO and LUMO energies were calculated for **PT** in both gas phase and various solvent environments (acetonitrile, chloroform, DMSO, ethanol, and water) using the same level of theory. Derived global reactivity parameters, including chemical potential, hardness, softness, electrophilicity index, and nucleophilicity index, were also calculated to assess the electronic behavior and stability of the molecule. Time-dependent DFT (TD-DFT) calculations were conducted to simulate the UV–visible absorption spectra in both gas and solvent phases. Dipole moment was computed for **PT** in the gas phase and in five solvents to evaluate its nonlinear optical properties. MEP analyses were conducted in both gas and solvent phases to evaluate how solvent polarity affects electronic distribution and reactive site localization. Natural population analysis (NPA), Mulliken population analysis, and natural bond orbital (NBO) analysis were performed at the B3LYP/cc-pVDZ level to determine atomic charge distributions, donor–acceptor interactions, and intramolecular charge delocalization. Electron localization function (ELF) and localized orbital locator (LOL) analyses were performed using Multiwfn software to visualize electron localization and bonding character. The molecular docking study was performed to investigate the binding interactions between **PT** and the human SGLT2–MAP17 protein complex (PDB ID: 8HEZ) [23]. The ligand structure was optimized using Avogadro software [24] and converted into PDB format. AutoDock 4.2 [25] and MGLTools were used for preparing the protein and ligand. Docking simulations were carried out using AutoDock 4.2 with the Lamarckian Genetic Algorithm (LGA). The grid box was defined as $60 \times 60 \times 60$ Å with a spacing of 0.553 Å, centered at coordinates $x = 66.85$, $y = 66.86$, and $z = 76.14$. Binding interactions were visualized and analyzed using BIOVIA Discovery Studio.

Results

Structural analysis

The molecular geometry of **PT** was optimized at the B3LYP/cc-pVDZ level of theory to obtain precise structural parameters. A comprehensive comparison of these parameters is provided in Table S1, Table S2, and Table S3 of the Supplementary Material. The optimized molecular structure of **PT** is depicted in Fig. 1. Among the calculated bond lengths, the longest is observed between atoms C2 and C3, measuring 1.4321 Å. In contrast, the shortest bond lengths are found between C1–C2 and C3–C4, both measuring 1.377 Å. The analysis of bond angles indicates that the S5–C4–C9 angle is the largest at 122.76°, while the smallest bond angle, H18–N17–C19, is recorded at 61.69°. Furthermore, the dihedral angles reveal notable variations, with H15–C14–C19–N17 exhibiting the largest dihedral angle of 179.9998° and H15–C14–N16–C12 displaying the smallest at 0.001°. Discrepancies between the computed and experimental structural parameters can be attributed to phase differences. While the experimental values in the literature

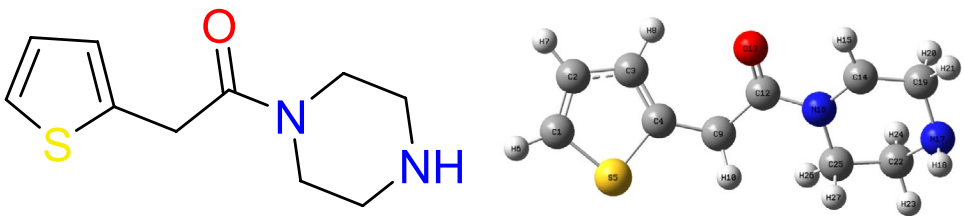

Fig. 1 Optimized structure of 1-(piperazin-1-yl)−2-(thiophen-2-yl) ethan-1-one (PT) at the B3LYP/cc-pVDZ level

correspond to the solid-state structure, the theoretical calculations presented here pertain to the gas-phase conformation.

Frontier molecular orbital (FMO) analysis

The FMO properties of the studied compound **PT** were analyzed in both gas and solvent phases, as summarized in Table 1. Figure 2 shows the FMOs of the compound **PT** for both the gas and solvent phases. The HOMO and LUMO energies provide insight into the molecule's electronic structure, stability, and reactivity [26, 27]. In the gas phase, the HOMO and LUMO values were found to be − 0.22380 eV and − 0.01053 eV, respectively, yielding an energy gap of 0.2133 eV. This energy gap slightly increased in solvent phases, indicating a solvent-induced stabilization effect. Among the solvents studied, chloroform exhibited the highest energy gap (0.2169 eV), while water, ethanol, acetonitrile, and DMSO showed similar trends with minor variations.

The ionization energy and electron affinity values, which are directly related to the HOMO and LUMO levels, were also determined. The ionization energy remained consistent across all phases, with a slight increase in solvent conditions. The electron affinity values, however, displayed minor fluctuations, with the highest value observed in water (− 0.01217 eV). These variations suggest that solvation influences the electron-withdrawing ability of the molecule.

Chemical hardness (η) and softness (S) parameters, which describe molecular stability and reactivity, revealed that the compound exhibits moderate chemical stability across all phases. The gas phase hardness value was calculated as 0.2185 eV, which increased slightly in the solvent phase. In contrast, the global softness values showed an inverse trend, decreasing slightly in solution. These findings are consistent with the notion that increased solvent interactions slightly rigidify the electronic properties of the molecule, reducing its reactivity.

The chemical potential (μ) and electronegativity (χ) values exhibited minimal changes, further supporting the relative stability of the molecule in different environments. The electronegativity values in the gas phase and solvent phases remained close, with only slight deviations observed in polar solvents such as water and acetonitrile.

One of the critical parameters evaluated was the electrophilicity index (ω), which provides insight into the molecule's ability to accept electrons [28]. The values across all phases remained relatively low (approximately 0.0310–0.0324 eV), indicating that the compound does not possess strong electrophilic behavior. Consequently, the nucleophilicity index (N), which is the inverse of electrophilicity, was found to be high, with values ranging from 30.86 to 32.25. This further confirms that the compound is a strong nucleophile and has a low tendency to act as an electron acceptor. The electron-accepting and electron-donating power parameters provided further insight into the redox behavior of the molecule [29]. The molecule displayed a relatively low electron-donating power, with values remaining stable across all phases. However, its electron-accepting power varied significantly, with the lowest value observed in chloroform (1.805) and the highest in water (3.434). This indicates that solvent polarity influences the compound's ability to accept electrons, which may have implications for its reactivity in different chemical environments.

Based on the FMO analysis, the findings suggest that the studied compound maintains its fundamental electronic properties across different phases. Furthermore, the compound **PT** demonstrates high nucleophilicity, moderate stability, and low electrophilicity, making it suitable for

Table 1 The FMO and GRP values of the **PT** in the gas and solvent phase

Property	Gas	Chloro form	Water	Ethanol	Acetonitrile	DMSO
E_{HOMO}	− 0.22380	− 0.22573	− 0.22779	− 0.22779	− 0.22778	− 0.22781
E_{LUMO}	− 0.01053	− 0.00885	− 0.01217	− 0.01165	− 0.01188	− 0.01201
Energy gap (ΔE)	0.2133	0.2169	0.2156	0.2161	0.2159	0.2158
Ionization energy ($I = -E_{HOMO}$)	0.22380	0.22573	0.22779	0.22779	0.22779	0.22781
Electron affinity ($A = -E_{LUMO}$)	0.01053	0.00885	0.01217	0.01165	0.01188	0.01201
Global hardness $\eta = (I - A)/2$)	0.2185	0.2213	0.2217	0.2220	0.2219	0.2218
Global softness ($S = 1/2\eta$)	4.5767	4.5188	4.5106	4.5045	4.5065	4.5086
Chemical potential ($\mu = -(I + A)/2$)	0.1172	0.1173	0.1200	0.1197	0.1198	0.1199
Electronegativity ($\chi = (I + A)/2$)	− 0.1172	− 0.1173	− 0.1200	− 0.1197	− 0.1198	− 0.1199
Electrophilicity index ($\omega = \mu^2/2\eta$)	0.0314	0.0310	0.0324	0.0322	0.0323	0.0324
Nucleophilicity index ($N = 1/\omega$)	31.84	32.25	30.86	31.05	30.95	30.86
Electron-accepting power ($\omega^+ = (I + 3A)^2/16(I - A)$)	2.599	1.805	3.434	3.139	3.268	3.341
Electron-donating power (($\omega^- = (3I + A)^2/16(I - A)$)	0.117	0.117	0.120	0.120	0.120	0.120

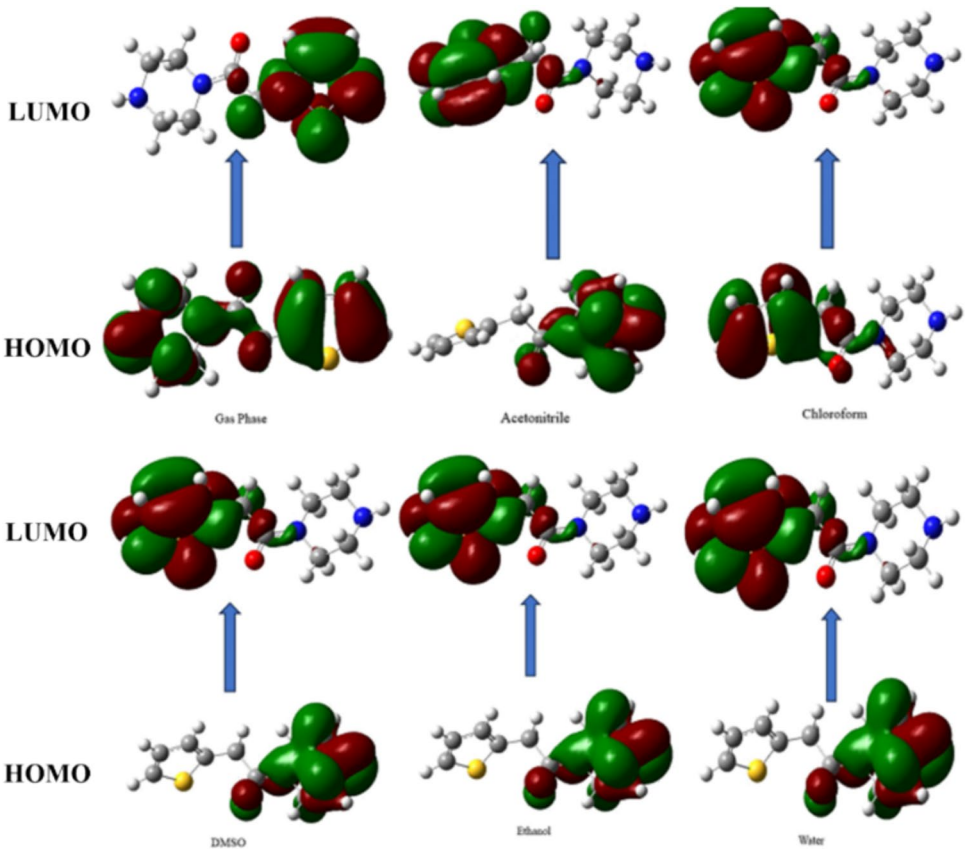

Fig. 2 FMOs of the studied compound **PT** in the gas and solvent phase

potential applications in pharmacological and therapeutic designs.

NLO analysis

The NLO properties of the **PT** molecule were evaluated at the B3LYP/cc-pVDZ level through dipole moment calculations in the gas phase and in various solvent environments. In the gas phase, the dipole moment of **PT** is found to be 1.2170 D. To assess solvent effects on the molecular polarity and hence its NLO response, dipole moments were calculated in five different solvents: acetonitrile (1.5567 D), chloroform (1.4730 D), dimethyl sulfoxide (DMSO, 1.5536 D), ethanol (1.5460 D), and water (1.5569 D). A significant increase in dipole moment values was observed upon solvation, indicating strong solvent–solute interactions that enhance charge delocalization within the molecule. Among the solvents studied, water induced the highest dipole moment, followed closely by acetonitrile and DMSO. This trend can be attributed to the high polarity and hydrogen-bonding capability of water, which strongly interacts with the **PT** molecule, leading to enhanced polarization. The observed increase in dipole moments in polar solvents correlates with an increase in NLO activity, as higher dipole moments generally suggest greater polarizability and charge-transfer characteristics, which are key indicators of efficient NLO behavior [30, 31].

The findings imply that solvent polarity plays a crucial role in modulating the electronic distribution within **PT**, which in turn amplifies its NLO response. Therefore, the **PT** molecule exhibits promising NLO properties, particularly in polar solvent media, highlighting its potential for optoelectronic and photonic applications.

UV–visible spectrum

The electronic transition parameters of the **PT** were investigated using the TD-DFT method in the gas phase and various solvent environments, including acetonitrile, chloroform, DMSO, ethanol, and water (Table 2 and Fig. 3). The computed transition energies, corresponding wavelengths, oscillator strengths, and primary molecular orbital contributions provide insights into the solvatochromic behavior of the compound.

In the gas phase, the first electronic excitation (S1) occurs at 5.3704 eV (230.86 nm) with an oscillator strength of 0.0511, predominantly characterized by H + 2 to LUMO (86%) transitions. The second (S2) and third (S3) states exhibit higher energy values at 5.5854 eV (221.98 nm) and 5.6544 eV (219.27 nm), respectively, with a complex mix of contributions from HOMO, HOMO + 1, and HOMO + 2 orbitals.

Table 2 Calculated electronic transition parameters of the compound **PT** in the gas and various solvent phases

Media	State	Energy	Wavelength	Oscillator strength	Contribution
Gas	S_1	5.3704 eV	230.86 nm	$f=0.0511$	HOMO—> LUMO (5%), H + 1—> LUMO (8%), H + 2—> LUMO 86%
	S_2	5.5854 eV	221.98 nm	$f=0.0947$	H + 1—> LUMO (69%), H + 1- > L + 1 (8%), H + 1—> L + 2 (3%), H + 2—> LUMO (4%), H + 2—> L + 1 (9%), H + 2—> L + 2 0.14062 (4%)
	S_3	5.6544 eV	219.27 nm	$f=0.0826$	H + 1—> LUMO (19%), H + 1—> L + 1 (2%), H + 1—> L + 2 (10%), H + 2—> LUMO (2%),H + 2—> L + 1 (37%), H + 2—> L + 2 (10%)
Acetonitrile	S_1	5.3880 eV	230.11 nm	$f=0.0009$	HOMO—> LUMO (9%) **H + 2—> LUMO (90%)**
	S_2	5.5555 eV	223.17 nm	$f=0.2370$	H − 2—> LUMO (6%), H − 1—> LUMO (5%),H + 1—> LUMO(84%)
	S_3	5.7107 eV	217.11 nm	$f=0.0368$	H − 2—> LUMO (7%), H − 1—> LUMO (74%), HOMO—> LUMO (3%), H + 1—> LUMO (6%), H + 1—> L + 3 (3%)
Chloroform	S_1	5.4519 eV	227.41 nm	$f=0.0010$	H − 1—> LUMO (3%), HOMO—> LUMO (8%),H + 1—> LUMO(88%)
	S_2	5.5459 eV	223.56 nm	$f=0.2416$	H − 2—> LUMO (6%), H − 1—> LUMO (4%), H + 2—> LUMO (84%)
	S_3	5.6845 eV	218.11 nm	$f=0.0049$	H − −2—> L + 1 (47%), H − 1—> L + 1 (36%), H + 2—> L + 1 (12%)
DMSO	S_1	5.3858 eV	230.20 nm	$f=0.0009$	HOMO—> LUMO (9%), **H + 2—> LUMO (90%)**
	S_2	5.5495 eV	223.41 nm	$f=0.2439$	H − 2—> LUMO (6%), H − 1—> LUMO (5%), H + 1- > LUMO (85%)
	S_3	5.7075 eV	217.23 nm	$f=0.0391$	H − 2—> LUMO (7%), H − 1—> LUMO (75%), HOMO—> LUMO (4%), H + 1—> LUMO (6%), H + 1—> L + 3 (3%)
Ethanol	S_1	5.3928 eV	229.91 nm	$f=0.0009$	HOMO—> LUMO (9%), H + 2—> LUMO (89%)
	S_2	5.5540 eV	223.23 nm	$f=0.2381$	H − 2—> LUMO (6%), H − 1—> LUMO (5%), H + 1—> LUMO (84%)
	S_3	5.7104 eV	217.12 nm	$f=0.0405$	H − 2—> LUMO (7%), H − 1—> LUMO (76%), H + 1—> LUMO (6%), H + 1—> L + 3 (3%)
Water	S_1	5.3819 eV	230.37 nm	$f=0.0009$	HOMO—> LUMO (9%), **H + 2—> LUMO (90%)**
	S_2	5.5566 eV	223.13 nm	$f=0.2366$	H − 2—> LUMO (6%), H − 1—> LUMO (6%), H + 1—> LUMO, (84%)
	S_3	5.7098 eV	217.14 nm	$f=0.0310$	H − 2—> LUMO (7%) H − 1—> 57 (69%), HOMO—> 57 (10%), H + 1—> LUMO (6%), H + 1—> L + 3 (2%), H + 2—> LUMO (3%)

Upon solvation, a general trend of slight redshifting in the S1 state is observed, as evident from the lower excitation energies compared to the gas phase. In polar solvents such as DMSO and water, the S1 transition remains nearly unchanged (5.3858 eV and 5.3819 eV, respectively) with minor reductions in oscillator strength. The most significant solvent-induced shift appears in chloroform, where S1 is at 5.4519 eV (227.41 nm), suggesting weaker solvent stabilization effects compared to more polar solvents.

A pronounced difference in oscillator strength (*f*) is observed among different environments. In acetonitrile, S2 exhibits the highest oscillator strength (0.2370), indicating a stronger electronic transition probability. Similarly, in chloroform, DMSO, ethanol, and water, S2 retains its dominant transition character with *f* values close to 0.24, highlighting the significant role of solvent polarity in modulating transition probabilities.

The molecular orbital contributions for S1 primarily involve HOMO to LUMO and H + 2 to LUMO transitions. In polar solvents, the dominant transition character is retained, with H + 2 → LUMO remaining the major contributor. However, in S2 and S3 states, the transition character becomes more complex, involving significant contributions from H − 2, H − 1, and H + 1 orbitals. Notably, in water, S3 transitions display increased mixing, with H − 1 → 57 (69%) and HOMO → 57 (10%) contributions, suggesting enhanced solvent interactions affecting excited-state characteristics.

The analysis reveals that solvent polarity influences both the excitation energies and transition probabilities of **PT**. While the S1 state remains relatively stable across solvents, the higher excited states exhibit noticeable variations in oscillator strength and orbital contributions. These findings suggest that the electronic properties of **PT** can be fine-tuned via solvent effects, which may have implications for its potential applications in optoelectronic or photophysical systems.

Molecular electronic potential (MEP) study

The molecular electrostatic potential (MEP) maps presented in Fig. 4 illustrate the electronic distribution of the studied molecule in different environments, including the gas phase and five distinct solvents (acetonitrile, chloroform, DMSO, ethanol, and water). These maps provide crucial insights into the charge distribution and potential interaction sites within the molecule, facilitating an understanding of solvent effects on electronic properties [32]. In the gas phase, the MEP map reveals a well-defined charge distribution, with regions of

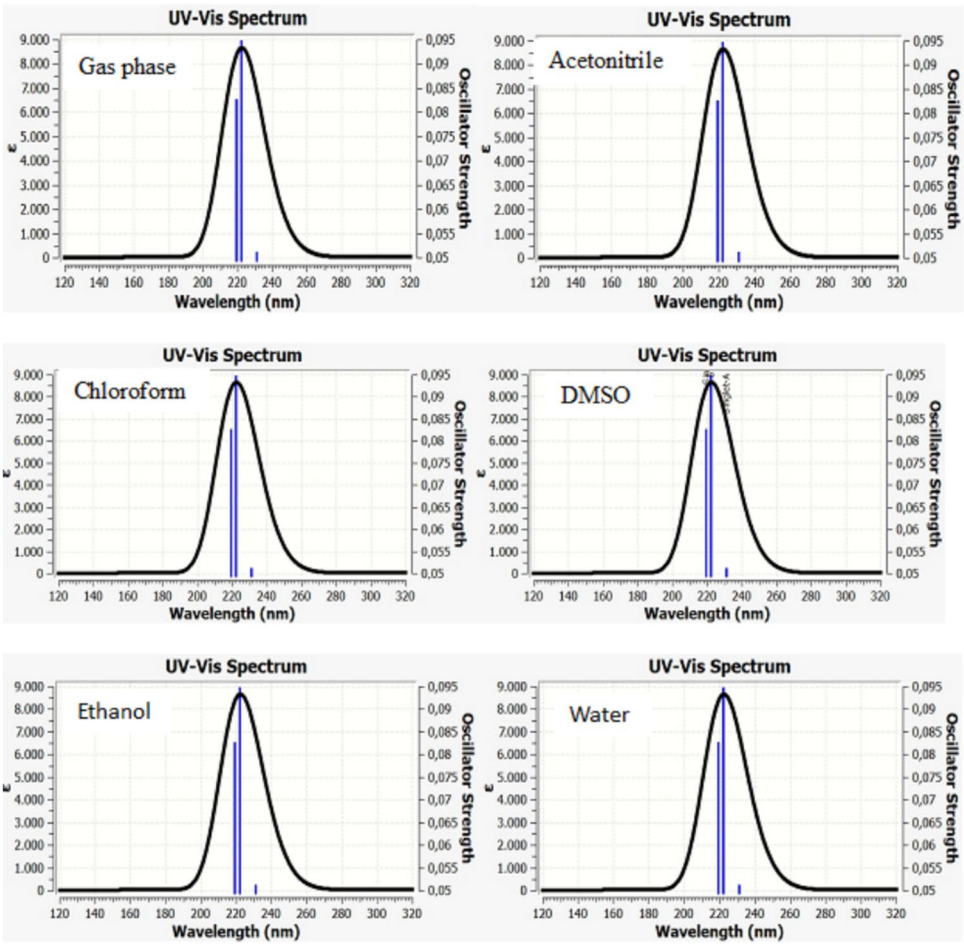

Fig. 3 Computed UV–Vis spectrum of **PT** in the gas and solvent phase

negative electrostatic potential (depicted in red) corresponding to electron-rich areas and regions of positive potential (in blue) indicating electron-deficient sites. In the **PT** molecule, the electron-rich sites are on the carbonyl oxygen and the sulfur in the thiophene ring, whereas the electron-poor sites are on the hydrogen bonded to the nitrogen in the piperazine ring. The distinct electrostatic potential distribution in the gas phase serves as a reference to evaluate the extent of solvent-induced perturbations. Conversely, in the solvent environment, the electrostatic potential map closely resembles that of the gas phase, with only minor shifts in charge distribution.

Natural population analysis (NPA)

Natural population analysis was performed to elucidate the charge distribution within the compound **PT**, offering insight into the electronic structure and the nature of bonding between atoms. The natural charges, along with core, valence, and Rydberg electron populations, are listed in Table 3. The analysis reveals that electronegative atoms such as oxygen and nitrogen exhibit significant negative natural charges, indicative of electron-rich centers. Notably, the oxygen atom (O13) carries the most negative charge at − 0.73519 e, while the nitrogen atoms N16 and N17 also bear substantial negative charges of − 0.49487 e and − 0.72576 e, respectively. This suggests these atoms may serve as strong hydrogen bond acceptors or sites for nucleophilic attack. Among the carbon atoms, C12 displays an unusually high positive charge (+ 0.66449 e), indicating significant electron deficiency in this region, potentially due to the influence of adjacent electronegative atoms or conjugation effects. Conversely, C9 shows the most negative charge (− 0.53377 e) among the carbons, suggesting its involvement in localized electron density, possibly stabilizing adjacent functionalities through hyperconjugation or resonance. The rest of the carbon framework carries modestly negative charges, with values generally ranging between − 0.16541 e and − 0.53377 e. The sulfur atom (S5) carries a positive charge of + 0.36810 e, reflecting partial electron withdrawal from its lone pairs, likely due to its involvement in delocalized π-systems or bonding interactions with surrounding atoms. As expected, all hydrogen atoms show positive natural charges, ranging from + 0.12158 e (H21) to + 0.33210 e (H18), indicating electron deficiency and their role in polar covalent bonds.

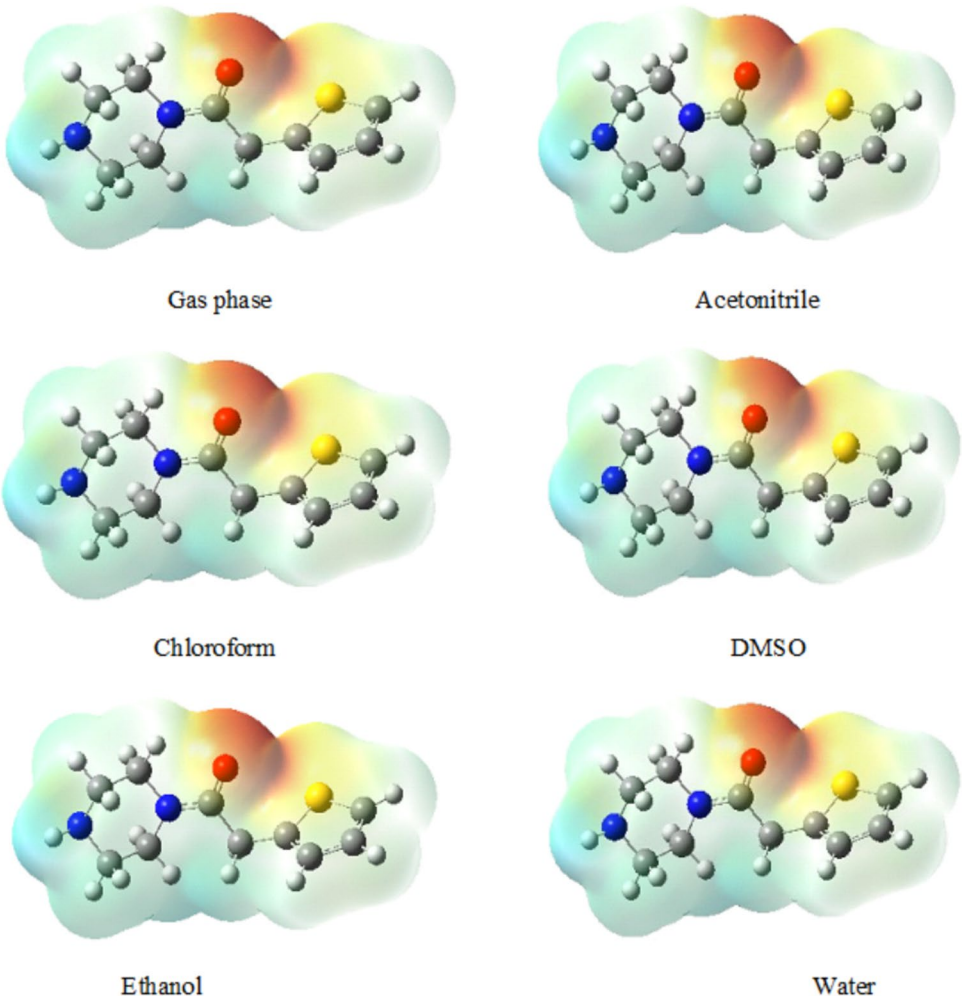

Fig. 4 MEP surface map of **PT** in the gas and solvent phase

Mulliken analysis

Mulliken population analysis was performed at the B3LYP/cc-pVDZ level to evaluate the electronic distribution and partial atomic charges in the **PT** molecule. The results, presented in Table 4, provide insight into the charge separation and potential reactive sites within the molecule. The analysis indicates that most hydrogen atoms exhibit slightly negative Mulliken charges, contrary to their typical behavior in many organic systems. This is particularly evident in H21 (−0.088581), H15 (−0.084940), and H23 (−0.058106), which may result from their bonding environment or adjacent electron-withdrawing groups. Such negative values suggest the presence of polar bonds or conjugated systems influencing charge delocalization. Among the non-hydrogen atoms, the oxygen atom (O13) possesses the highest negative charge (−0.378053), aligning with its high electronegativity and strong electron-withdrawing character. This atom likely contributes significantly to the molecule's overall polarity and reactivity profile. Similarly, nitrogen atoms N16 and N17 show substantial negative charges of −0.164123 and −0.232059, respectively, reinforcing their roles as electron-rich centers potentially capable of forming hydrogen bonds or participating in nucleophilic interactions. Several carbon atoms are also negatively charged, particularly C14 (−0.247339) and C4 (−0.207655), indicating regions of electron density that may stabilize interactions or delocalize electron density across the molecular framework. In contrast, positively charged carbon atoms such as C12 (+0.112480), C19 (+0.125549), and C25 (+0.115070) reflect electron-deficient sites, which might play roles in electrophilic interactions or conjugation effects within the aromatic or heterocyclic structure. The sulfur atom (S5) carries a small positive charge of +0.064308, consistent with its role as a bridging or electron-donating species in delocalized systems. The relatively small magnitude of this charge suggests moderate electron sharing with adjacent atoms. Overall, the Mulliken population analysis highlights a non-uniform charge distribution in the **PT** molecule, marked by regions of both electron richness and deficiency. These findings are in agreement with the natural population analysis results and support the electronic features expected from the molecular

Table 3 Natural population analysis of compound **PT**

Atom No	Natural charge	Core	Valence	Rydberg	Total
C1	−0.44619	1.99901	4.42834	0.01884	6.44619
C2	−0.26657	1.99892	4.25240	0.01526	6.26657
C3	−0.28149	1.99874	4.26372	0.01903	6.28149
C4	−0.16541	1.99892	4.14440	0.02209	6.16541
S5	0.36810	9.99886	5.59335	0.03969	15.63190
H6	0.22814	0.00000	0.76961	0.00225	0.77186
H7	0.21940	0.00000	0.77772	0.00288	0.78060
H8	0.26331	0.00000	0.73078	0.00591	0.73669
C9	−0.53377	1.99906	4.51737	0.01735	6.53377
H10	0.22050	0.00000	0.77490	0.00460	0.77950
H11	0.23195	0.00000	0.75821	0.00984	0.76805
C12	0.66449	1.99918	3.28201	0.05432	5.33551
O13	−0.73519	1.99980	6.72589	0.00950	8.73519
C14	−0.47168	1.99925	4.44143	0.03099	6.47168
H15	0.18626	0.00000	0.80802	0.00572	0.81374
N16	−0.49487	1.99916	5.48170	0.01401	7.49487
N17	−0.72576	1.99957	5.71064	0.01556	7.72576
H18	0.33210	0.00000	0.66029	0.00762	0.66790
C19	−0.22504	1.99925	4.20952	0.01628	6.22504
H20	0.17699	0.00000	0.81883	0.00418	0.82301
H21	0.12158	0.00000	0.86395	0.01447	0.87842
C22	−0.21363	1.99928	4.19532	0.01903	6.21363
H23	0.18431	0.00000	0.81017	0.00551	0.81569
H24	0.21478	0.00000	0.77917	0.00605	0.78522
C25	−0.21947	1.99925	4.20614	0.01409	6.21947
H26	0.18306	0.00000	0.80905	0.00789	0.81694
H27	0.18410	0.00000	0.80786	0.00804	0.81590

structure, offering valuable information for understanding the molecule's reactivity and interaction potential.

Natural bond orbital (NBO) analysis

Natural bond orbital (NBO) analysis was carried out at the B3LYP/cc-pVDZ level to investigate the hyperconjugative interactions and intramolecular charge delocalization in the **PT** molecule (Table 5). This analysis provides a quantitative insight into donor–acceptor interactions and the resulting stabilization energies ($E^{(2)}$), offering a deeper understanding of the molecule's electronic structure. The second-order perturbation theory analysis indicates several significant interactions between filled (donor) and vacant (acceptor) orbitals, especially those involving π and lone-pair orbitals. The most prominent interaction was observed between the π bonding orbital of the C1–C2 bond and the π* antibonding orbital of the C3–C4 bond, with a high stabilization energy of 90.79 kJ/mol. This strong delocalization suggests extended π-conjugation across the molecular framework, which likely contributes to the molecule's electronic delocalization and potential reactivity. Another notable $\pi \rightarrow \pi^*$ interaction is seen between the C3–C4 and C9–H11 orbitals ($E^{(2)} = 1.37$ kJ/mol), further reflecting the delocalized nature of the π-system. The π(C12–O13) → π*(C12–O13) transition also displayed a significant stabilization energy of 17.46 kJ/mol, indicating lone pair resonance contributions to the conjugated system. Lone pair (LP) interactions also play a critical role in the stabilization of the **PT** molecule. The most significant LP interaction arises from the lone pair on nitrogen N16 donating into the π*(C12–O13) orbital, resulting in a stabilization energy of 60.84 kJ/mol. This high value confirms the strong $n \rightarrow \pi^*$ delocalization, enhancing conjugation and potentially modulating reactivity at the carbonyl site. Similarly, lone pair donation from N17 to σ*(C22–C25) and from S5 to σ*(C3–C4) contributes to overall molecular stabilization. The $\sigma \rightarrow \sigma^*$ interactions were also prevalent throughout the molecule, with stabilization energies ranging from ~ 1.0 to over 5.0 kJ/mol. For instance, the σ(C2–C3) → σ*(C4–C9) interaction had a notable energy of 5.58 kJ/mol, while the σ(C3–H8) → σ*(C4–S5) interaction showed a stabilization energy of 5.87 kJ/mol. These hyperconjugative interactions highlight the delocalization of bonding electrons into adjacent antibonding orbitals, a feature contributing to structural rigidity and electronic distribution.

Table 4 Mulliken population analysis of compound **PT**

Atom	Mulliken charge	Atom	Mulliken charge	Atom	Mulliken charge
1 C	−0.124441	10 H	−0.027458	19 C	0.125549
2 C	0.072166	11 H	0.009350	20 H	−0.049549
3 C	0.075566	12 C	0.112480	21 H	−0.088581
4 C	−0.207655	13 O	−0.378053	22 C	0.110677
5 S	0.064308	14 C	−0.247339	23 H	−0.058106
6 H	−0.029753	15 H	−0.084940	24 H	−0.001411
7 H	−0.055578	16 N	−0.164123	25 C	0.115070
8 H	−0.027477	17 N	−0.232059	26 H	−0.030422
9 C	0.109396	18 H	0.037708	27 H	−0.025326

Table 5 Natural bond orbital analysis of compound **PT**

Donor (*i*)	Type	Acceptor (*j*)	Type	$E^{(2)}$ (kJ/mol)	$E(j)$-$E(i)^{b}$ (a.u.)	$F(i, j)$
BDC1–C2	σ	BD*C1–H6	σ*	2.18	1.19	0.045
		BD*C2–C3	σ*	2.62	1.28	0.052
		BD*C2–H7	σ*	1.70	1.19	0.040
		BD*C3–H8	σ*	3.06	1.23	0.055
		BD*C3–C4	π*	13.28	0.32	0.061
BDC1–S5	σ	BD*C1–C2	σ*	0.66	1.27	0.026
		BD*C2–H7	σ*	4.93	1.12	0.066
		BD*C4–C9	σ*	3.37	1.10	0.054
BDC1–H6	σ	BD*C1–C2	σ*	1.72	1.17	0.040
		BD*C2–C3	σ*	3.18	1.11	0.053
		BD*C4–S5	σ*	0.74	0.78	0.021
BDC2–C3	σ	BD*C1–C2	σ*	2.74	1.27	0.053
		BD*C1–H6	σ*	4.71	1.12	0.065
		BD*C2–H7	σ*	1.06	1.12	0.031
		BD*C3–C4	σ*	2.86	1.29	0.054
		BD*C3–H8	σ*	1.22	1.16	0.034
		BD*C4–C9	σ*	5.58	1.10	0.070
BDC2–H7	σ	BD*C1–C2	σ*	1.24	1.14	0.034
		BD*C1–S5	σ*	4.57	0.75	0.052
		BD*C3–C4	σ*	2.57	1.16	0.049
BDC3–C4	σ	BD*C2–C3	σ*	2.91	1.27	0.054
		BD*C2–H7	σ*	3.20	1.17	0.055
		BD*C3–H8	σ*	1.97	1.21	0.044
		BD*C4–C9	σ*	3.52	1.15	0.057
		BD*C9–H10	σ*	0.92	1.18	0.029
BDC3–C4	π	BD*C1–C2	π*	18.88	0.28	0.067
		BD*C9–H11	σ*	2.85	0.72	0.042
		BD*C9–C12	σ*	0.86	0.68	0.022
BDC3–H8	σ	BD*C1–C2	σ*	2.44	1.11	0.047
		BD*C2–C3	σ*	0.54	1.06	0.021
		BD*C3–C4	σ*	2.29	1.13	0.046
		BD*C4–S5	σ*	5.87	0.72	0.058
BDC4–S5	σ	BD*C1–C2	σ*	0.52	1.27	0.023
		BD*C1–H6	σ*	3.14	1.12	0.053
		BD*C3–C4	σ*	0.53	1.29	0.023
		BD*C3–H8	σ*	4.20	1.16	0.062
		BD*C9–C12	σ*	1.41	1.08	0.035
BDC4–C9	σ	BD*C2–C3	σ*	2.35	1.19	0.047
		BD*C3–C4	σ*	3.88	1.27	0.063
		BD*C9–H10	σ*	0.62	1.10	0.023
		BD*C9–H11	σ*	0.64	1.09	0.024
		BD*C9–C12	σ*	0.97	1.06	0.029
		BD*C12–O13	π*	1.41	0.76	0.033
		BD*C12–N16	σ*	1.00	1.21	0.032
BDC9–H10	σ	BD*C3–C4	σ*	4.91	1.12	0.066
		BD*C12–O13	π*	3.31	1.06	0.053
		BD*C22–C25	σ*	0.72	0.90	0.023
BDC9–H11	σ	BD*C3–C4	σ*	0.57	1.10	0.022
		BD*C3–C4	π*	5.05	0.51	0.048
		BD*C4–S5	σ*	1.04	0.69	0.024
		BD*C12–O13	π*	3.26	0.59	0.044

Table 5 (continued)

Donor (*i*)	Type	Acceptor (*j*)	Type	$E^{(2)}$ (kJ/mol)	$E(j)$-$E(i)^{b}$ (a.u.)	$F(i, j)$
		BD*C12–N16	σ*	2.33	1.04	0.044
BDC9–C12	σ	BD*C3–C4	π*	1.14	0.61	0.025
		BD*C4–S5	σ*	3.84	0.79	0.049
		BD*C4–C9	σ*	1.71	1.01	0.037
		BD*C9–H10	σ*	0.80	1.03	0.026
		BD*C9–H11	σ*	0.56	1.03	0.021
		BD*C14–N16	σ*	4.32	1.02	0.059
BDC12–O13	σ	BD*C9–H10	σ*	0.98	1.35	0.033
		BD*C9–C12	σ*	0.54	1.31	0.024
		BD*C12–N16	σ*	0.81	1.47	0.031
		BD*N16–C25	σ*	2.43	1.27	0.050
BDC12–O13	π	BD*C4–C9	σ*	1.30	0.78	0.028
		BD*C12–O13	π*	1.85	0.46	0.029
		BD*C12–N16	σ*	0.68	0.91	0.023
		BD*N16–C25	σ*	0.68	0.72	0.020
BDC12–N16	σ	BD*C12–O13	σ*	0.73	1.34	0.028
		BD*C14–N16	σ*	2.56	1.22	0.050
		BD*N16–C25	σ*	1.81	1.15	0.041
		BD*C22–C25	σ*	0.70	1.19	0.026
BDC14–H15	σ	BD*N16–C25	σ*	4.39	0.77	0.052
		BD*N17–C19	σ*	4.74	0.77	0.054
		BD*C9–C12	σ*	3.86	1.04	0.057
		BD*C12–N16	σ*	2.98	1.20	0.054
		BD*N16–C25	σ*	1.11	1.00	0.030
		BD*C19–H20	σ*	1.96	1.13	0.042
		BD*C25–H26	σ*	0.58	1.08	0.022
		BD*C25–H27	σ*	1.00	1.10	0.030
BDC14–C19	σ	BD*C12–N16	σ*	2.00	1.10	0.043
		BD*N17–H18	σ*	0.64	1.00	0.022
		BD*C19–H20	σ*	0.76	1.04	0.025
		BD*C19–H21	σ*	0.64	1.01	0.023
		BD*N17–H18	σ*	0.64	1.00	0.022
		BD*C19–H20	σ*	0.76	1.04	0.025
BDN16–C25	σ	BD*C12–O13	σ*	3.60	1.23	0.060
		BD*C12–N16	σ*	1.58	1.24	0.040
		BD*C14–H15	σ*	1.13	1.25	0.034
		BD*C14–N16	σ*	1.27	1.11	0.034
		BD*C22–H23	σ*	1.12	1.14	0.032
BDN17–H18	σ	BD*C14–C19	σ*	0.65	1.06	0.024
		BD*C19–H20	σ*	1.16	1.05	0.031
		BD*C22–H24	σ*	3.24	1.05	0.052
BDN17–C19	σ	BD*C14–H15	σ*	1.70	1.20	0.040
		BD*C22–H23	σ*	1.92	1.08	0.041
BDN17–C22	σ	BD*C19–H21	σ*	0.64	1.14	0.024
		BD*C25–H26	σ*	1.32	1.12	0.035
BDC19–H20	σ	BD*C14–N16	σ*	4.14	0.88	0.054
		BD*N17–H18	σ*	1.13	0.89	0.028
		BD*N17–C22	σ*	1.08	0.83	0.027
BDC19–H21	σ	BD*N17–C22	σ*	2.52	0.83	0.041
BDC22–H23	σ	BD*N16–C25	σ*	3.88	0.85	0.051
		BD*N17–C19	σ*	3.73	0.84	0.050

Table 5 (continued)

Donor (*i*)	Type	Acceptor (*j*)	Type	$E^{(2)}$ (kJ/mol)	$E(j)$-$E(i)^b$ (a.u.)	$F(i, j)$
BDC22–H24	σ	BD*N17–H18	σ*	3.31	0.93	0.050
		BD*C25–H27	σ*	2.77	0.93	0.045
BDC22–C25	σ	BD*C12–N16	σ*	3.05	1.15	0.054
		BD*C25–H26	σ*	0.61	1.03	0.022
		BD*C25–H27	σ*	0.58	1.04	0.022
BDC25–H26	σ	BD*C14–N16	σ*	0.90	0.92	0.026
		BD*N17–C22	σ*	3.84	0.88	0.052
BDC25–H27	σ	BD*C14–N16	σ*	2.05	0.93	0.039
		BD*C22–H24	σ*	2.72	0.98	0.046
LPS5	n	BD*C1–C2	σ*	2.29	1.25	0.048
		BD*C3–C4	σ*	2.40	1.27	0.049
LPO13	n	BD*C9–C12	σ*	2.13	1.02	0.042
		BD*C12–N16	σ*	1.77	1.17	0.041
LPC14	n	BD*C12–O13	π*	1.34	0.21	0.016
		BD*C12–N16	σ*	5.12	0.66	0.055
		BD*N17–C19	σ*	2.39	0.46	0.032
		BD*C19–H20	σ*	1.09	0.60	0.024
		BD*C19–H21	σ*	12.05	0.57	0.078
		BD*C22–H23	σ*	1.55	0.56	0.028
		BD*C25–H27	σ*	0.71	0.56	0.019
LPN16	n	BD*C12–O13	σ*	2.98	0.74	0.046
		BD*C12–O13	π*	60.84	0.29	0.120
		BD*C12–N16	σ*	1.29	0.75	0.030
		BD*C14–N16	σ*	1.69	0.63	0.032
		BD*C14–C19	σ*	3.85	0.69	0.051
		BD*C19–H20	σ*	0.78	0.68	0.023
		BD*C22–C25	σ*	0.56	0.59	0.018
		BD*C25–H26	σ*	6.66	0.63	0.065
		BD*C25–H27	σ*	3.16	0.65	0.045
LPN17	n	BD*C14–C19	σ*	2.68	0.76	0.041
		BD*C19–H20	σ*	3.72	0.76	0.048
		BD*C22–H23	σ*	0.73	0.72	0.021
		BD*C22–H24	σ*	1.29	0.75	0.028
		BD*C22–C25	σ*	8.72	0.66	0.068
		BD*C25–H26	σ*	0.56	0.71	0.018
BD*C1–C2	π*	BD*C3–C4	π*	90.79	0.02	0.075
BD*C3–C4	π*	BD*C9–H11	σ*	1.37	0.41	0.054
		BD*C9–C12	σ*	0.69	0.38	0.034
BD*C12 – O13	π*	BD*C4–C9	σ*	2.27	0.32	0.049
		BD*C9–H11	σ*	2.32	0.34	0.051
		BD*C12–O13	σ*	17.46	0.45	0.156
		BD*N16–C25	σ*	0.62	0.26	0.023

BD* 2-center bond, *LP* for 1-center valence lone pair, *BD 2-center antibond

Electron localization function (ELF) and localized orbital locator (LOL) analysis

Topological analyses of the ELF and LOL for the compound **PT** were conducted using the Multiwfn software package. The ELF distribution was visualized using a color gradient ranging from blue to red within the 0.000–1.000 Bohr interval, where red regions indicate areas of high electron localization, and blue corresponds to regions with low electron

density. Similarly, the LOL mapping employed a color scale spanning 0.000 to 0.800 Bohr, with red hues marking zones of maximal localization. Figure 5 presents the contour-filled ELF and LOL maps of the **PT** molecule. Enhanced electron localization was particularly evident in red-shaded areas surrounding the C–C, C–N, and C–O bonds, suggesting the presence of strongly localized electron clouds, especially around terminal hydrogen atoms bonded to carbon. Conversely, the blue regions observed around various carbon and nitrogen atoms reflect zones of electron delocalization, indicating a less localized electronic environment within those regions.

Figure 5 displays the ELF map of compound **PT**, which clearly distinguishes between regions of bonding and non-bonding electron density. Areas with high ELF values, indicated in red, are especially prominent around hydrogen atoms and along C–C bonds, reflecting zones of significant electron localization. In contrast, regions with lower ELF values, visualized in blue, form pronounced rings surrounding carbon and nitrogen atoms, indicative of delocalized electronic structures. The corresponding LOL map of compound **PT** in Fig. 5 further supports these findings. Red rings encircling hydrogen atoms signify regions of concentrated core electron density. The centers of these atoms appear white, a visual cue that the electron density exceeds the upper bound of the color scale (0.8), consistent with core regions near the nucleus. Additionally, red areas located between carbon atoms in the LOL map represent bonding regions with a high degree of electron localization, suggesting a strong tendency for electron pair formation. The presence of blue rings around carbon, nitrogen, and oxygen atoms indicates zones of electron delocalization, commonly associated with π-conjugated systems or lone pair interactions.

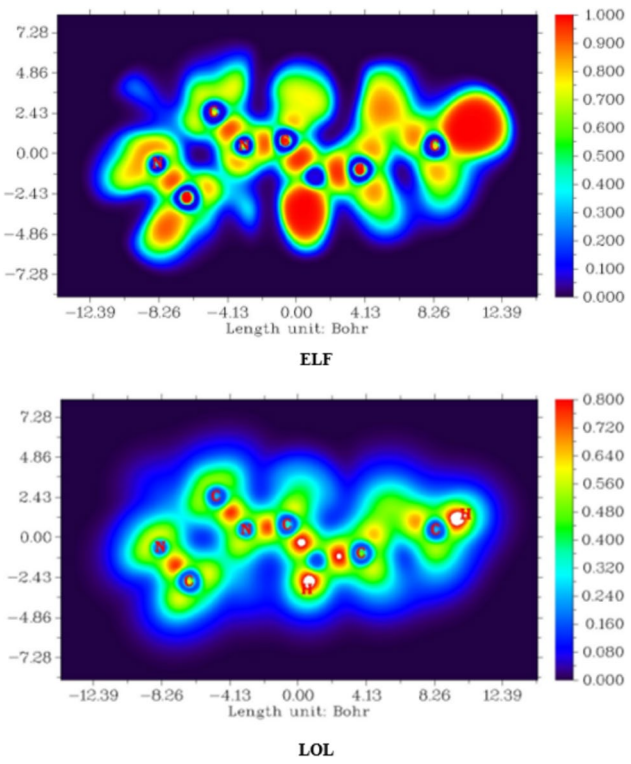

Fig. 5 ELF and LOL color-filled map of compound **PT**

Molecular docking

Molecular docking was employed as a fundamental in silico approach to evaluate the interaction of the test compound, **PT**, with the human SGLT2-MAP17 protein complex, providing insights into potential binding modes and affinity. The crystallographic structure of the SGLT2-MAP17 complex in association with dapagliflozin (PDB ID: 8HEZ) was retrieved from the RCSB Protein Data Bank (https://www.rcsb.org/) and used as the target for docking studies [23].

The **PT** ligand was initially constructed in 2D and subsequently optimized in 3D using Avogadro software, with energy minimization applied prior to conversion into the PDB format. The protein and ligand structures were further processed using AutoDock 4.2 and MGLTools to generate PDBQT files suitable for docking simulations. Protein preparation included the removal of water molecules, the addition of polar hydrogens, and the assignment of Kollman charges. The torsional flexibility of the ligand was appropriately assigned to allow for rotational freedom during docking. Docking simulations were carried out using the LGA protocol. Grid parameters were set to $60 \times 60 \times 60$ Å^3 with a grid spacing of 0.553 Å, centered at coordinates $x = 66.85$, $y = 66.86$, and $z = 76.14$. These parameters defined the active site of the SGLT2-MAP17 complex.

In this study, the interactions between SGLT2-MAP17 complex and **PT** molecule were analyzed, and binding energies were calculated within the scope of in silico molecular docking studies. In addition, potential binding interactions were investigated by re-docking **Dapagliflozin** co-crystallized with SGLT2-MAP17 complex, and these results were compared with **PT** molecule.

Figure 6 and Table 6 show the structural interaction of relocated **Dapagliflozin** with human SGLT2-MAP17 complex (PDB: 8HEZ). **Dapagliflozin** was observed to exhibit a strong binding interaction with SGLT2-MAP17. A conventional hydrogen bond was observed between the ligand and Phe98 (2.24 Å), Lys321(2.21 Å), and Asn75 (2.24 Å). The π-donor hydrogen bond interactions were detected between Tyr290 with a bond length of 3.13 Å. The π-cation interaction was observed with residue Hıs80 (4.95 Å). π-sigma interactions were observed with Tyr290 (3.38 Å) and Val157 (3.33 Å). Alkyl interactions were observed with Lys154 (4.08 Å) and Ile397 (5.16 Å). π-Alkyl interactions

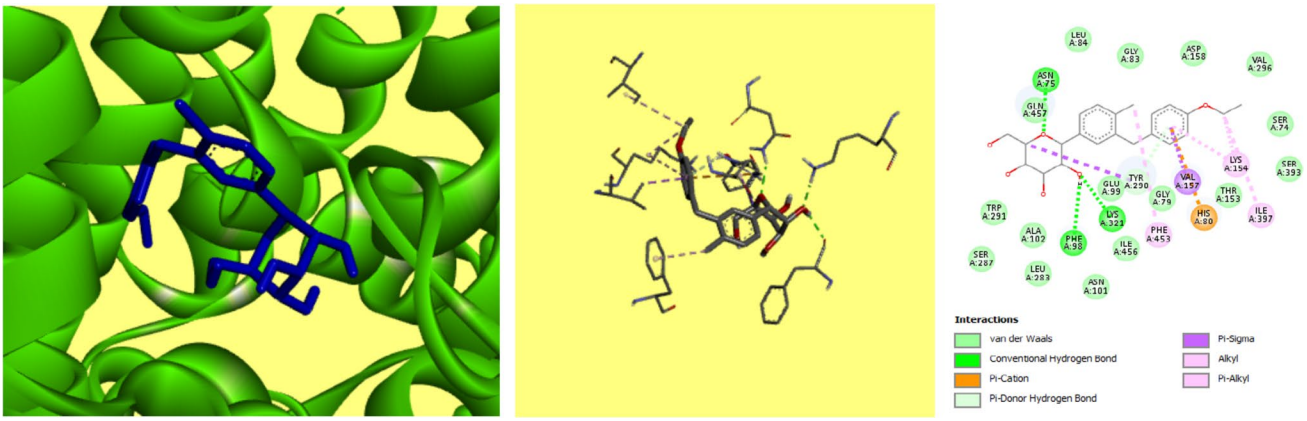

Fig. 6 The protein–ligand interaction site of **Dapagliflozin**. Interactions between ligand and protein are shown on the left as colored dashed lines. 2D interaction graphs are also presented on the right

Table 6 The protein–ligand interaction with selected residues and binding energy value of **Dapagliflozin**

Compound	Interaction type	Residues	Distance	Binding energy (kcal/mol)
Dapagliflozin	Conventional hydrogen bond	Phe98	2.24	**−8.79**
		Lys321	2.11	
		Asn75	2.24	
	π-Donor hydrogen bond	Tyr290	3.13	
	π-Cation	Hıs80	4.95	
	Alkyl	Lys154	4.08	
		Ile397	5.16	
	π-Sigma	Tyr290	3.38	
		Val157	3.33	
	π-Alkyl	Lys154	5.21	
		Phe453	4.68	
	Van der Waals	Leu84, Gly83, Asp158, Val296, Ser74, Ser393, Thr153, Gly79, Glu99, Ile456, Asn101, Leu283, Ala102, Ser287, Trp291, Gln457		

were observed with residues Lys154 (5.21 Å) and Phe453 (4.68 Å). Van der Waals interactions were observed among Leu84, Gly83, Asp158, Val296, Ser74, Ser393, Thr153, Gly79, Glu99, Ile456, Asn101, Leu283, Ala102, Ser287, Trp291, and Gln457. All significant binding interactions are summarized in Table 6.

The molecular docking results of **PT** revealed the best binding energy of − 6.93 kcal/mol corresponding to an estimated inhibition constant (Ki) of 8.26 mM (Table 7, Fig. 7), indicating that **PT** engages in various stabilizing interactions within the binding pocket. A conventional hydrogen bond was observed between the ligand and Asp454 (1.76 Å) and Gln457 (2.97 Å). The π–π T-shaped interactions were detected between the thiophene ring and the side chains of Phe453 and His80, with bond distances of 4.98 Å and 5.01 Å, respectively. Additionally, π-alkyl interactions were formed between the ligand and Leu84 (4.82 Å) and Phe98 (5.24 Å). All significant binding interactions are summarized in Table 7. These findings suggest that **PT** exhibits moderate binding affinity toward the SGLT2-MAP17 complex. The relatively low inhibition constant implies a potential inhibitory effect on the biological activity of the target protein, which may be of therapeutic relevance. The nature and strength of the observed noncovalent interactions indicate that **PT** could serve as a promising lead compound in the development of selective SGLT2 inhibitors.

Table 7 The protein–ligand interaction with selected residues and binding energy value of **PT**

Compound	Interaction type	Residues	Distance	Binding energy (kcal/mol)
1-(Piperazin-1-yl)−2-(thiophen-2-yl)ethan-1-one	Conventional hydrogen bond	Asp454	1.76	**− 6.93**
		Gln457	2.97	
	π–π T-shaped	Phe453	4.98	
		His80	5.01	
	π-Alkyl	Leu84	4.82	
		Phe98	5.24	
	Van der Waals	Leu274, Tyr526, Val157, Gly79, Gly83, Thr87, Val95		

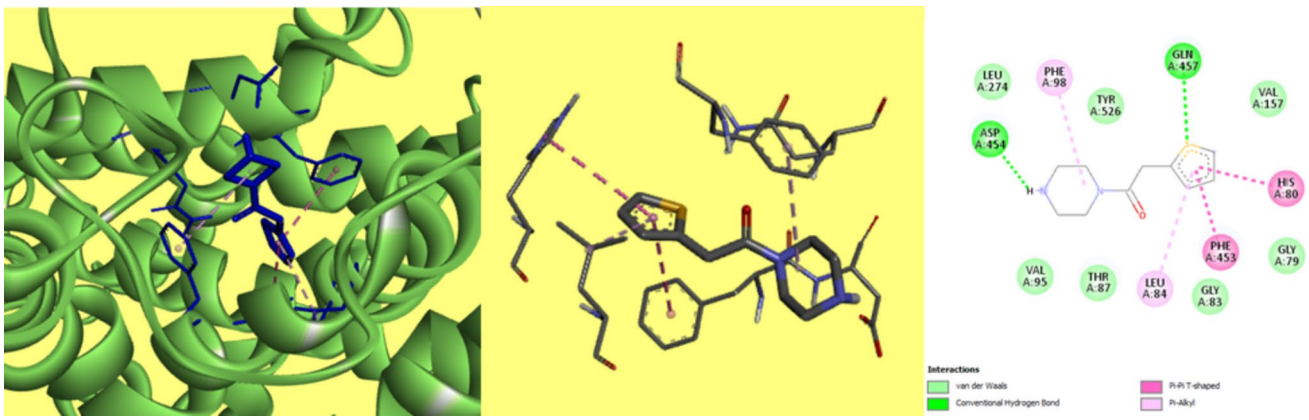

Fig. 7 The protein–ligand interaction site of **PT**. Interactions between ligand and protein are shown on the left as colored dashed lines. 2D interaction graphs are also presented on the right

Conclusions

This study presents an integrated computational investigation of 1-(piperazin-1-yl)−2-(thiophen-2-yl) ethan-1-one (**PT**), combining quantum chemical calculations and molecular docking to evaluate its structural, electronic, optical, and pharmacological features. Geometry optimization and frontier molecular orbital (FMO) analyses, performed at the B3LYP/cc-pVDZ level, revealed that **PT** possesses a moderate HOMO–LUMO energy gap, supporting its electronic stability and reactivity. Global reactivity parameters indicated high nucleophilicity and low electrophilicity, suggesting favorable interaction potential with biological targets.

Solvent-dependent dipole moment and UV–visible spectral analyses demonstrated enhanced non-linear optical (NLO) behavior and solvatochromic shifts, especially in polar environments. These properties are indicative of strong solvent-molecule interactions and suggest the compound's potential applicability in optoelectronic systems. Complementary analyses, including MEP, ELF, and LOL, highlighted regions of electron density localization and potential reactive sites, while NPA, Mulliken, and NBO analyses confirmed substantial charge delocalization and donor–acceptor interactions contributing to molecular stability.

In the docking studies with SGLT2–MAP17 protein complex (PDB: 8HEZ), **PT** molecule exhibited a binding energy of − 6.93 kcal/mol, revealing significant non-covalent interactions such as hydrogen bonds and π–π stacking. This suggests that **PT** exhibits a promising binding affinity towards the target protein. This value, when compared to the binding affinity of **Dapagliflozin** (− 8.79 kcal/mol) re-docked with human SGLT2–MAP17 complex, indicates that **PT** also has a remarkable binding potential. The docking data suggest that PT molecule may exhibit a binding activity similar to Dapagliflozin.

Overall, the obtained findings suggest that **PT** is a structurally and electronically viable candidate as an SGLT2 inhibitor; therefore, it should be evaluated in future in vitro and in vivo pharmacological studies.

Supplementary Information The online version contains supplementary material available at https://doi.org/10.1007/s11224-025-02555-x.

Author contribution Özlem Gündoğdu Aytaç Conceptualization, Methodology, Writing–original draft. Abdurrahman Atalay Writing–original draft, Formal analysis. Ebrar Nur Özkan Software, Formal analysis. Sertan Aytaç Investigation, Writing– original draft.

Data availability The data that support the findings of this study are available from the corresponding author upon reasonable request.

Declarations

Competing interest The authors declare that they have no known competing financial interests or personal relationships that could have appeared to influence the work reported in this paper.

References

1. Magliano DJ, Boyko EJ (2021) IDF Diabetes Atlas 10th edition scientific committee. IDF Dıabetes Atlas, 10th ed., International Diabetes Federation, Brussels. http://www.ncbi.nlm.nih.gov/books/NBK581934/ (accessed October 10, 2023).
2. Cho NH, Shaw JE, Karuranga S, Huang Y, Fernandes JD da R, Ohlrogge AW, Malanda B (2018) IDF diabetes Atlas: global estimates of diabetes prevalence for 2017 and projections for 2045. Diabetes Res Clin Pract 138: 271–281. https://doi.org/10.1016/j.diabres.2018.02.023.
3. Mathers CD, Loncar D (2006) Projections of global mortality and burden of disease from 2002 to 2030. PLoS Med 3:e442. https://doi.org/10.1371/journal.pmed.0030442
4. Feng X, Astell-Burt T (2017) Impact of a type 2 diabetes diagnosis on mental health, quality of life, and social contacts: a longitudinal study. BMJ Open Diab Res Care 5. https://doi.org/10.1136/bmjdrc-2016-000198.
5. Berbudi A, Rahmadika N, Tjahjadi AI, Ruslami R (2025) Type 2 diabetes and its ımpact on the ımmune system. http://www.eurekaselect.com (n.d.). https://www.eurekaselect.com/article/101842 (accessed March 25, 2025).
6. De Rosa S, Arcidiacono B, Chiefari E, Brunetti A, Indolfi C, Foti DP (2018) Type 2 diabetes mellitus and cardiovascular disease: genetic and epigenetic links. Front Endocrinol 9. https://doi.org/10.3389/fendo.2018.00002.
7. Daryabor G, Atashzar MR, Kabelitz D, Meri S, Kalantar K (2020) The effects of type 2 diabetes mellitus on organ metabolism and the ımmune system. Front Immunol 11. https://doi.org/10.3389/fimmu.2020.01582.
8. Siddiqui K, George TP, Joy SS, Alfadda AA (2022) Risk factors of chronic kidney disease among type 2 diabetic patients with longer duration of diabetes. Front Endocrinol 13. https://doi.org/10.3389/fendo.2022.1079725.
9. Sayour AA, Oláh A, Ruppert M, Barta BA, Merkely B, Radovits T (2024) Effect of pharmacological selectivity of SGLT2 inhibitors on cardiovascular outcomes in patients with type 2 diabetes: a meta-analysis. Sci Rep 14:2188. https://doi.org/10.1038/s41598-024-52331-w
10. Hasan I, Rashid T, Jaikaransingh V, Heilig C, Abdel-Rahman EM, Awad AS (2024) SGLT2 inhibitors: beyond glycemic control. J Clin Transl Endocrinol 35:100335. https://doi.org/10.1016/j.jcte.2024.100335
11. Zhang A, Kalil R, Marzec A, Coulter SA, Virani S, Patel K, Segar V (2024) Cardiovascular disease management with sodium-glucose cotransporter-2 ınhibitors in patients with type 2 diabetes: a cardiology primer, M.W. Tex Heart Inst J 51. https://doi.org/10.14503/THIJ-23-8375.
12. Nespoux J, Vallon V (2020) Renal effects of SGLT2 inhibitors: an update. Curr Opin Nephrol Hypertens 29:190. https://doi.org/10.1097/MNH.0000000000000584
13. Diker Cohen T, Polansky A, Bergman I, Ayada G, Babich T, Akirov A, Steinmetz T, Dotan I (2025) Safety of sodium-glucose cotransporter 2 inhibitors in kidney transplant recipients with diabetes mellitus. Diabetes Metab 51:101627. https://doi.org/10.1016/j.diabet.2025.101627
14. Yang XP, Lai D, Zhong XY, Shen H-P, Huang YL (2014) Efficacy and safety of canagliflozin in subjects with type 2 diabetes: systematic review and meta-analysis. Eur J Clin Pharmacol 70:1149–1158. https://doi.org/10.1007/s00228-014-1730-x
15. Joshi SS, Singh T, Newby DE, Singh J (2021) Sodium-glucose co-transporter 2 inhibitor therapy: mechanisms of action in heart failure. Heart 107:1032–1038. https://doi.org/10.1136/heartjnl-2020-318060
16. Kumar N, Kumar B, Ashique S, Yasmin S, Venkatesan K, Islam A, Ghosh S, Sahu A, Bhui U, Ansari M Y (2025) A critical review on SGLT2 inhibitors for diabetes mellitus, renal health, and cardiovascular conditions, Diabetes Res Clin Pract. 221. https://doi.org/10.1016/j.diabres.2025.112050.
17. Siddiqi TJ, Cherney D, Siddiqui HF, Jafar TH, Januzzi JL, Khan MS, Levin A, Marx N, Rangaswami J, Testani J, Usman MS, Wanner C, Zannad F, Butler J (2025) Effects of sodium-glucose cotransporter-2 inhibitors on kidney outcomes across baseline cardiovascular-kidney-metabolic conditions: a systematic review and meta-analyses. J Am Soc Nephrol 36:242. https://doi.org/10.1681/ASN.0000000000000491
18. Preda A, Montecucco F, Carbone F, Camici GG, Lüscher TF, Kraler S, Liberale L (2024) SGLT2 inhibitors: from glucose-lowering to cardiovascular benefits. Cardiovasc Res 120:443–460. https://doi.org/10.1093/cvr/cvae047
19. Lopaschuk GD, Verma S (2020) Mechanisms of cardiovascular benefits of sodium glucose co-transporter 2 (SGLT2) inhibitors: a state-of-the-art review. JACC: Basic Transl Sci 5: 632–644. https://doi.org/10.1016/j.jacbts.2020.02.004.
20. Medetalibeyoğlu H, Atalay A, Sağlamtaş R, Manap S, Ortaakarsu AB, Ekinci E, Yüksek H, Tüzün B (2025) Int J Biol Macromol 306:141350. https://doi.org/10.1016/j.ijbiomac.2025.141350
21. Ayaz M, Gündoğdu Ö, Aytaç S, Erdem B, Çiftçi H, Erdogdu Y (2022) Microwave-assisted synthesis, characterizations, antimicrobial activities, and DFT studies on some pyridine derived Schiff bases. J Mol Struct 1269:133791. https://doi.org/10.1016/j.molstruc.2022.133791
22. Idris S, Jan F, Waheed M, Alam A, Ibrahim M, AlAsmari AF, Alasmari F, Bo L, Khan M (2024) Multifaceted bioactivity of thiosemicarbazide derivatives: synthesis, characterization, and DFT investigations on inhibition of α-amylase, hydroxyl radical scavenging, and iron chelating activities with molecular docking insights. J Mol Struct 1304:137669. https://doi.org/10.1016/j.molstruc.2024.137669
23. Shahab S, Kumar R, Sheikhi M, Ihnatovich Z, Siniutsich J, Koroleva E, Filippovich L, Auhustsinovich A, Makhakhei M, Stati M, Hui W, Khancheuski M, Borzehandani MY (2024) Synthesis, modeling, bioactivity, docking, binding energy analysis of new effective piperazine derivatives as effective drug candidates for treatment of Parkinson's disease. Anal Chem Lett 14:638–653. https://doi.org/10.1080/22297928.2024.2397798
24. Woldegiorges K, Belay A, Kebede A, Abebe T (2021) Estimating the ground and excited state dipole moments of levofloxacin and norfloxacin drugs using solvatochromic effects and computational work. J Spectrosc 7214182. https://doi.org/10.1155/2021/7214182.

25. Thiaré DD, Khonté A, Diop A, Cissé L, Coly A, Tine A, Delattre F (2015) Determination of ground and excited state dipole moments of amino-benzimidazole by solvatochromic shift methods and theoretical calculations. J Mol Liq 211:640–646. https://doi.org/10.1016/j.molliq.2015.07.071
26. Akyıldırım O, Medetalibeyoğlu H, Oğuz E, Aras A, Atalay A, Korkmaz A, Beytur M, Türkan F, Yüksek H (2023) Novel Mannich bases derived from 1,2,4-triazoles: design, synthesis, characterization, and glutathione S-transferase inhibition properties investigations. J Mol Struct 1293:136321. https://doi.org/10.1016/j.molstruc.2023.136321
27. Hiraizumi M, Akashi T, Murasaki K, Kishida H, Kumanomidou T, Torimoto N, Nureki O, Miyaguchi I (2024) Transport and inhibition mechanism of the human SGLT2–MAP17 glucose transporter. Nat Struct Mol Biol 31:159–169. https://doi.org/10.1038/s41594-023-01134-0
28. Becke AD (1988) Density-functional exchange-energy approximation with correct asymptotic behavior. Phys Rev A 38:3098–3100. https://doi.org/10.1103/PhysRevA.38.3098
29. Lee C, Yang W, Parr RG (1988) Development of the Colle-Salvetti correlation-energy formula into a functional of the electron density. Phys Rev B 37:785–789. https://doi.org/10.1103/PhysRevB.37.785
30. Frisch MJ, Trucks GW, Schlegel HB, Scuseria GE, Robb M A, Cheeseman JR, Scalmani G, Barone V, Petersson GA, Nakatsuji H, Li X, Caricato M, Marenich AV, Bloino J, Janesko B G, Gomperts R, Mennucci B, Hratchian H P, Ortiz JV, Izmaylov AF, Sonnenberg J L, Williams-Young D, Ding F, Lipparini F, Egidi F, Goings J, Peng B, Zheng G, Liang W, Hada M, Ehara M, Toyota K, Fukuda R, Hada M, Ehara M, Toyota K, Fukuda R, Hasegawa J, Ishida M, Nakajima T, Ishida M, Nakajima T, Honda Y, Kitao O, Nakai H, Vreven T, Throssell K, Montgomery J A, Peralta J E, Ogliaro F, Bearpark M J, Heyd J J, Brothers E N, Kudin K N, Staroverov V N, Keith T A, Kobayashi R, Normand J, Raghavachari K, Rendell A P, Burant J C, Iyengar S S, Tomasi J, Cossi M, Millam J M, Klene M, Adamo C, Cammi R, Ochterski J W, Martin R L, Morokuma K, Farkas O, Foresman J B, Fox D J (n.d.) Gaussian 16, *Gaussian Inc.*
31. Hanwell MD, Curtis DE, Lonie DC, Vandermeersch T, Zurek E, Hutchison GR, Cheminf J (2012) Avogadro: an advanced semantic chemical editor, visualization, and analysis platform. J Cheminformatics 4:17. https://doi.org/10.1186/1758-2946-4-17
32. Morris GM, Huey R, Lindstrom W, Sanner MF, Belew RK, Goodsell DS, Olson AJ (2009) AutoDock4 and AutoDockTools4: automated docking with selective receptor flexibility. J Comput Chem 30:2785–2791. https://doi.org/10.1002/jcc.21256